Simulation of the formation of antihydrogen in a nested Penning trap: effect of positron density

S Jonsell[1]**, D P van der Werf**[1]**, M Charlton**[1] **and F Robicheaux**[2]

[1] Department of Physics, School of Physical Sciences, Swansea University, Singleton Park, Swansea SA2 8PP, UK
[2] Department of Physics, Auburn University, AL 36849-5311, USA

E-mail: B.S.Jonsell@Swansea.ac.uk

Abstract
Detailed simulations of antihydrogen formation have been performed under the conditions of the ATHENA experiment, using several densities of the positron plasma in the range $n_e = 5 \times 10^{13}$ m^{-3} to 10^{15} m^{-3}. The simulations include only collisional effects, typically resulting in the formation of weakly bound antihydrogen via the three-body process, $e^+ + e^+ + \bar{p} \rightarrow \bar{H} + e^+$. (Radiative processes, which are much slower than collisional effects, are neglected.) The properties of these weakly bound anti-atoms are affected not only by further collisions in the plasma but also by the inherent electric fields. The role of field ionization in influencing the distribution of binding energies of the antihydrogen is clarified and the mechanism for this process in the strong B-field nested Penning trap used in the experiment is elucidated. The fate of antihydrogen is explained and the properties of the population detected after having reached the wall of the Penning trap electrodes, as well as those field ionized, are recorded. We find that the yield of detected antihydrogen varies with positron density roughly as $n_e^{1.7}$, rather than the n_e^2 expected from the underlying formation process. As n_e is increased, antihydrogen formation is sufficiently rapid that epithermal effects begin to play an important role. In general, the simulated timescales for antihydrogen formation are much shorter than those found from the experiment.

1. Introduction and motivation

Cold antihydrogen was formed in pioneering experiments at CERN, first by the ATHENA collaboration [1] and then by ATRAP [2], via the controlled mixing of antiprotons and positrons in specially tailored Penning-type traps. This has established a new field of atomic physics and triggered a flurry of theoretical activity aimed at elucidating the basic physics underlying the antihydrogen experiments in an effort to interpret several of the observations. This area has recently been reviewed [3]. Currently, two experiments, ALPHA [4] and ATRAP [5], are attempting to confine antihydrogen by forming it inside a magnetic minimum (Ioffe–Pritchard type [6]) neutral atom trap. Plans for antihydrogen experiments are also underway within the ASACUSA collaboration [7]. Recently the AEGIS experiment, focusing on the gravitational interaction of antihydrogen, was formally approved for operation at CERN [8]. For these ventures to be successful, and to enable progress to be made towards using antihydrogen for various tests of fundamental physics (see e.g. [9]), it is essential that the properties of the anti-atoms upon formation (for example, binding energies and speeds) are understood and, if possible, controlled.

Antihydrogen can be formed by a number of routes [9], including the two mechanisms shown below. These are direct spontaneous radiative recombination as

$$\bar{p} + e^+ \rightarrow \bar{H} + h\nu, \tag{1}$$

with a rate Γ_{srr}, and three-body recombination given by

$$\bar{p} + e^+ + e^+ \rightarrow \bar{H} + e^+, \tag{2}$$
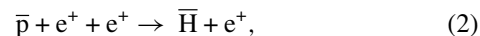
with a rate Γ_{tbr}. The physics of these reactions is explored further elsewhere [9–11]. Briefly, however, in the steady state the reactions have very different dependences upon the

temperature, T_e, and density, n_e, of the positron plasma, with $\Gamma_{srr} \propto n_e T_e^{-0.63}$ and $\Gamma_{tbr} \propto n_e^2 T_e^{-4.5}$. Thus, at first sight, it would appear to be easy to distinguish between them. Furthermore, the two reactions produce very different distributions of bound states. The radiative process is a dipole-allowed free-bound transition which favours capture of the positron into strongly bound states. By contrast, the three-body case is expected to favour weakly bound antihydrogen since the reaction is essentially an elastic encounter of two positrons in the vicinity of the antiproton. Thus, energy transfers around $k_B T_e$ are likely, which sets the scale for the probable binding energies. Such weakly bound states are expected to be dramatically influenced by the ambient fields of the Penning traps.

From the experimental perspective, it was found that antihydrogen could be formed very efficiently [12] upon merging positrons and antiprotons in a nested Penning trap [13]. Here the applied magnetic field was in the Tesla range, and typical electric fields in the trap were in the region of tens of V cm^{-1}. In the case of ATHENA, the trap electrodes were held at a temperature of around 15 K (to which the positrons cool by the emission of synchrotron radiation in the strong applied magnetic field), and typical positron plasma densities were in the 10^{14}–10^{15} m^{-3} range [14, 15]. Furthermore, ATHENA could heat their positrons by the application of a radio frequency (rf) signal to one of the electrodes surrounding the plasma; indeed, when the heating was applied such that positron temperatures of several thousand kelvin were obtained, it was found that antihydrogen formation was effectively suppressed [1, 12]. This served as a convenient background signal [12].

ATHENA also performed some experiments in which antihydrogen formation was monitored as T_e was increased in a systematic manner [16]. It was found that the antihydrogen yields, at least at temperatures > 100 K, fell as $T_e^{-0.7\pm0.2}$, and no dramatic rise was apparent at lower T_e, as would have been expected from the three-body reaction. However, the rates of detected antihydrogen atoms (sometimes in excess of 400 s^{-1}) were around an order of magnitude greater than those characteristic of the radiative process. (Reference [17] obtained the radiative formation rate $1.55 \times 10^{-16} T_e^{-0.63} n_e$ s^{-1}, with T_e in kelvin and n_e in m^{-3}, which with the experimental parameters in [16] gives 48 s^{-1}.)

In a recent contribution, ATHENA has published an analysis of an experiment in which they modulated antihydrogen production by the pulsed application of rf fields [18]. With the rf on, antihydrogen formation was suppressed. When the field was removed, antihydrogen formation resumed with a time constant determined by the cooling rate of the positrons in the 3 T applied magnetic field, convoluted with the temperature dependence of the antihydrogen formation rate. By directly measuring the former, they were able to extract the latter, finding a dependence as $T_e^{-1.1\pm0.5}$, over a wide range of T_e. Despite the fact that these two experiments found exponents of T_e consistent with the radiative process, the signal rates pointed to a dominance of the three-body reaction. Clearly, there are inconsistencies here, which so far have not been resolved.

Various aspects of antihydrogen formation have been considered in earlier theoretical work. Glinsky and O'Neil calculated the rate of three-body recombination in the limit of an infinite magnetic field, assuming a stationary antiproton [19]. Antihydrogen formation is a multi-step process, requiring a succession of collisions before the anti-atom is stable against ionization. Glinsky and O'Neil [19] found that anti-atoms bound by more than $\sim 10 k_B T_e$ are stable against collisional ionization. Robicheaux and Hanson simulated the same rate at various magnetic fields and other conditions relevant for the ATRAP and ATHENA experiments [20]. In that work, the antiproton was allowed to move freely, and the drift of the positrons, which is due to the electric field of the plasma, was included. The results of both these calculations were consistent with the $T_e^{-9/2}$ scaling of the three-body recombination rate, albeit with a pre-factor depending on the magnetic-field strength. However, [21] found that this temperature scaling is only valid in a steady-state situation, where the antiproton is immersed in the positron plasma for a time longer than the time required for recombination. This assumption does not hold true in a nested Penning trap, and the model predictions therefore have limited relevance to the current antihydrogen experiments. In a nested Penning trap arrangement, the antiprotons pass to and fro across the positron plasma, such that the reactions are arrested in nature every time the antiproton leaves the plasma, having to start anew the next time it enters the positrons. Since the anti-atom needs time to build up binding energy, this has the effect of lowering the mean binding energy of the anti-atom and increasing its kinetic energy over that expected from T_e. Such an observation is consistent with results from both ATHENA [22] and ATRAP [23], though the latter has been subject to a re-interpretation [24]; see also [3].

Classical trajectory simulations of single positrons in the combination of a strong magnetic field and the electric field from a stationary antiproton have also revealed that metastable antihydrogen states with negative binding energy (i.e. unbound) can be formed in two-body collisions [25]. Such metastable states can be stabilized through a collision with a second positron, a process that is implicitly included in the three-body rates calculated in the present paper. Antihydrogen formation has also been studied using molecular dynamics calculations [26, 27].

Over the past few years, a number of theoretical studies have been performed examining different properties of highly excited antihydrogen as formed from positron plasmas. This includes calculations of the magnetic moments [28], the radiative cascade of highly excited antihydrogen [29] and field ionization [30]. In a very recent paper, the change of the binding energy in collisions between highly excited antihydrogen and positrons, assuming a stationary antiproton, was studied in some detail [31]. The results in [31] confirm that the time needed to establish a steady state with a $T_e^{-9/2}$ scaling of the formation rate is much longer than the actual time that the antiproton spends in the plasma in experiments.

We have been motivated by the insights provided by the early simulations to extend them to investigate some of the aforementioned phenomena in greater detail. In this paper

we integrate, for the first time, the various aspects of the antihydrogen formation process into a simulation of the entire evolution of the experimental events. A detailed description of the simulation method is given below in section 2. Briefly, the simulations start with the injection of antiprotons into the nested Penning trap. We follow the trajectories of the antiprotons back and forth through the positron plasma. Whilst traversing the plasma, the antiproton slows due to collisions with positrons and also undergoes three-body collisions that potentially lead to the formation of antihydrogen. The trajectories of any antihydrogen atoms formed are likewise calculated until they either are ionized or leave the plasma. Outside the plasma, the trajectory of the antihydrogen atom is calculated until it either reaches the detector or alternatively is ionized by the electric fields present in the trap (in the latter case the antiproton is followed for 0.3 ms to make sure that it does not return to the positron plasma). No previous simulations include all these stages of the formation process. In this way, we obtain distributions of positions, velocities and binding energies of detected antihydrogen atoms. We also obtain results for the time dependence of the antihydrogen formation process.

In the simulations we use a realistic representation of the trap geometry, the electric and magnetic fields inside the trap and the positron plasma. Specifically we have chosen to use parameters characteristic of the ATHENA experiment [1], i.e. magnetic field $B = 3$ T, plasma temperature $T_e = 15$ K and plasma densities n_e varying between 5×10^{13} m^{-3} and 10^{15} m^{-3}.

Our results establish a number of physical effects that, at least qualitatively, apply independently of the simulation parameters used. In section 3.2 we extract rates for antihydrogen formation. We find that the density scaling of the antihydrogen detection rate deviates from the simple n_e^2 dependence predicted for three-body recombination in steady state. Other results include a mechanism for field ionization which has not been considered previously (section 3.3), a density dependence of the binding energies of antihydrogen surviving to the detector (section 3.4), a radial drift of the antiprotons (section 3.5), loss of antiprotons due to field ionization of antihydrogen formed at large trap radii (section 3.6) and epithermal formation of antihydrogen (section 3.7).

2. Simulations and underlying physics

Our simulations are based on classical trajectories of antiprotons, as previously described in [3, 20, 21, 28, 29]. Quantum mechanical effects are expected to play a role only at small interparticle distances, characteristic of much more tightly bound antihydrogen than that considered in this work. Before we integrate the classical equations of motion we must determine the electric and magnetic field configuration in the nested Penning trap. As mentioned above, we use electric and magnetic fields characteristic of the nested Penning trap developed by the ATHENA experiment [1]. In a Penning trap, the radial confinement is provided by a constant magnetic field directed along the axis of the trap, which in our case has the
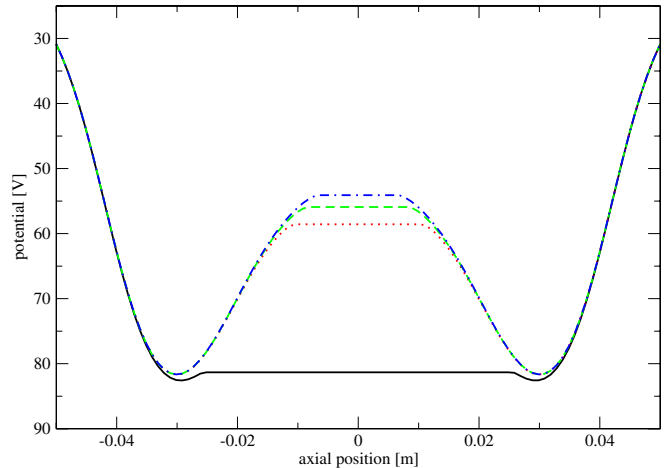

Figure 1. Axial electric potential for various n_e and N_e : (——) $n_e = 10^{15}$ m^{-3} and $N_e = 1.2 \times 10^8$; $n_e = 5 \times 10^{13}$ m^{-3} and (·····) $N_e = 2.8 \times 10^7$, (− − −)$N_e = 1.4 \times 10^7$ and (— · —)$N_e = 7 \times 10^6$.

strength $B = 3$ T. The axial confinement of the plasma comes from the electric field. This field has two sources, the voltages set on the cylindrical electrodes surrounding the trap and the space charge of the positron plasma. Thus, for a given number of positrons N_e and peak density of the plasma n_e, the electric field and the spatial profile of the plasma are inter-related and have to be determined by solving Poisson's equation self-consistently for both quantities. In addition, the (small) effect of the finite temperature of the plasma is taken into account by using a standard Maxwell–Boltzmann distribution. The procedure for solving these equations is well established and outlined, e.g., in [32].

The electric field inside the trap is then determined by the space charge of the positrons and from the voltages applied to the electrodes. Inside the plasma, the axial electric field vanishes, while the radial electric field, $\mathbf{E}_r$, is given by [32]

$$\mathbf{E}_r = \frac{n_e e r}{2\epsilon_0}\hat{\rho}, \qquad (3)$$

where r is the distance from the axis of the system, $\hat{\rho}$ is the unit vector directed radially away from the axis of the cylindrical trap and e and ϵ_0 have their usual meanings. Typical axial electric potentials in the trap are depicted in figure 1 at some of the extreme values of n_e and N_e used in the simulations. The positrons are trapped at the flat local minimum of the electric potential. The side-wells on both sides of this local minimum provide the necessary confinement of the positrons, but here antiprotons, as discussed below, may also get trapped.

In the experiments, antiprotons are injected into the plasma by manipulating the voltages on the electrodes, and thereby temporarily opening up the electric potential on one side. The antiprotons will therefore initially have an axial kinetic energy of a few eV. In most of our simulations, antiprotons are initialized with a kinetic energy of 2 eV directed along the axis of the trap, whilst in the transverse direction a thermal distribution at 15 K is assumed. However, in some simulations, we use antiprotons initialized from a 15 K distribution both axially and transversely, in order to explicitly study antihydrogen formation in the equilibrium situation.
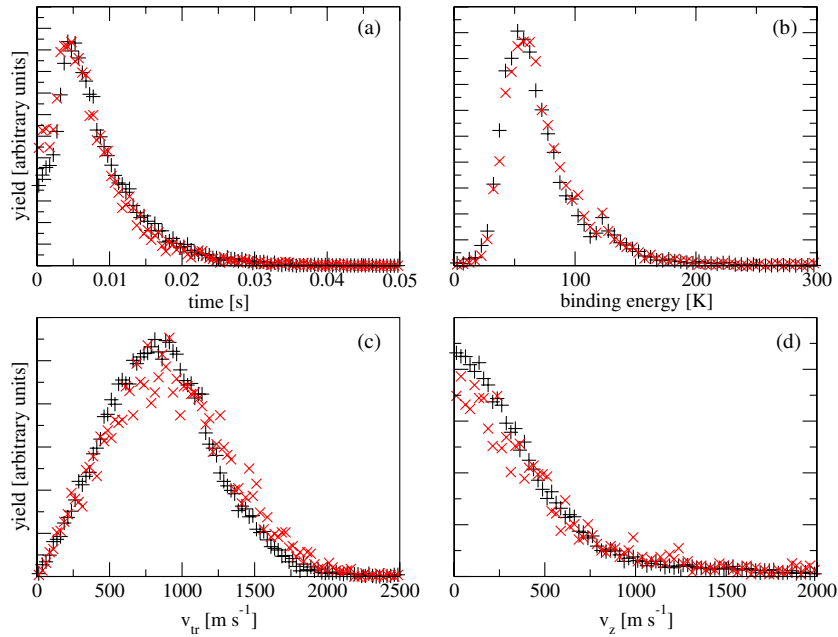
Figure 2. Results using different requirements for the binding energy of a formation event, (+) $E_b > k_B T_e$ and (×) $E_b > 2k_B T_e$, for $n_e = 2 \times 10^{14}$ m^{-3} and $T_e = 15$ K. (a) The time dependence of antihydrogen detection; (b) the binding energy distributions of the detected antihydrogen; (c) the antihydrogen speed distributions in the transverse plane and (d) their axial counterparts.

As the antiproton traverses the plasma, it collides with positrons and may thus form antihydrogen. These collisions are treat by defining a box of a predefined size (see below) around the antiproton. For each time step the statistical probability for a positron to enter through one of the faces of the box is calculated. Only the motion of the positrons inside this box is explicitly solved and the rest of the plasma is considered as a continuous medium. The trajectories of the antiproton and any positrons present are obtained by integrating Newton's equation of motion for the particles subject to the familiar electromagnetic, or Lorentz, force:

$$\mathbf{F} = q(\mathbf{E} + \mathbf{v} \times \mathbf{B}), \tag{4}$$

where $q = \pm e$ for positrons/antiprotons and $\mathbf{v}$ is the velocity of the particle. The electric field is the sum of the trapping field described above and the field from the Coulomb interaction between the particles. The equations of motion are integrated numerically using a Runge–Kutta method with a time step monitored by the requirement of energy conservation. In contrast to [20, 21], the guiding centre approximation is not employed for the motion of the positrons. The trajectories of positrons are calculated until they leave through one of the faces of the box. We define an antihydrogen atom simply as a state with a single positron inside the box, and its lifetime as the time the positron stays inside the box. Thus, the metastable states discussed by Correa *et al* [25] and true bound states with positive binding energy are treated on an equal footing.

Most collisions between the antiproton and positrons are not important for antihydrogen formation because the energy exchange between the particles is small. Only antihydrogen with binding energy $\gtrsim k_B T_e$ can be stable against ionization. The corresponding classical radius of the anti-atom is then $\lesssim r_T = e^2/(4\pi \epsilon_0 k_B T_e)$, which also gives the maximum

interparticle separation at which formation can occur. The calculation is therefore divided into two parts: in the first stage formation events are calculated until a binding energy of $k_B T_e$ is reached, and in the second stage these formation events are used in a simulation including the full motion of the antiproton. In the first stage a box around the antiproton (see above) with a side-length equal to $10 r_T$ is used, which for $T_e = 15$ K gives 1.1 μm. For numerical efficiency this stage of the collision is treat by approximating the antiproton to be stationary. This can be justified since the collision time is short compared to the time the antiproton needs to traverse the plasma. For binding energies greater than $k_B T_e$ the full dynamics of the antiproton is calculated. In this stage, we use a side-length of the box around the antiproton equal to the average positron separation in the plasma.

The stationary-antiproton approximation will only cause errors in the observed time, velocity, position and energy distributions if it is applied to antihydrogen atoms which otherwise would have been able to reach the detector without being field ionized. As is discussed below in section 3.4, for $T_e = 15$ K antihydrogen with binding energy less than $k_B T_e$ cannot survive field ionization. To further check the effect of this approximation, we compare the distributions obtained from our standard simulation (stationary antiproton down to the binding energy $k_B T_e$) to those from a simulation using a more restrictive approximation with the corresponding binding energy equal to $2k_B T_e$. (Comparing to a less restrictive approximation would require a considerably larger computational effort.) The results (at the density $n_e = 2 \times 10^{14}$ m^{-3}) are shown in figure 2. We observe no significant change in any of the distributions. However, the ratio of the total number of detected antihydrogen atoms to the total number of simulated antiproton trajectories increases from

0.34 to 0.46. This change is understood. The remaining antiprotons are lost through the formation of very weakly bound antihydrogen atoms, which ionize outside the plasma, as will be discussed in section 3.2. When only antihydrogen atoms bound by $2k_B T_e$ are allowed to move outside the plasma, there will be fewer weakly bound antihydrogens, leading to a smaller number of lost antiprotons. The properties of more tightly bound antihydrogen which survive to the detector are, however, not affected.

The interaction between the antiproton and the positron plasma also gives a slowing of its velocity. The stopping power of ions in a strongly magnetized plasma has been investigated by Nersisyan *et al* [33]. We use their results to calculate the velocity-dependent kinetic energy loss of the antiprotons. The results in [33] were derived under the assumption that the number of positrons in a sphere with radius equal to the Debye length $\lambda_D = \sqrt{\epsilon_0 k_B T_e/(n_e e^2)}$ is much larger than 1. At $T_e = 15$ K this number varies from 11 at $n_e = 5 \times 10^{13}$ m^{-3} to 2.5 at $n_e = 10^{15}$ m^{-3}. Hence, at the highest density we are approaching the limit of validity of this theory. The associated uncertainty will, however, only have a limited impact on the time needed to slow the antiproton down to thermal energies—a time which anyway carries an uncertainty due to the variation of the initial kinetic energy for different experimental conditions. It will have no impact on the long-time behaviour of either antihydrogen formation rates or the time, velocity, position and energy distributions that we use as observables. A recent study used an alternative method to calculate the rate of slowing of the antiprotons [34]. Here, the average momentum transfer in antiproton–positron collisions was simulated as a function of impact parameter. This gives a more accurate description of low-energy collisions, but does not take any plasma effects into account. For the parameter values in our simulations, the results in [33] and in [34] give slowing rates of similar magnitude.

The antiproton trajectories are calculated until they either, in the form of antihydrogen, reach the detector at the cylindrical electrodes surrounding the trap or are trapped outside the positron plasma. For anti-atoms reaching the detector, we record observables such as the time and position of detection, speeds and binding energies. Also the time and position distributions of trapped antiprotons are recorded. Although impossible to observe experimentally, we have found it instructive to study antiproton properties at intermediate times, such as when leaving the positron plasma in the form of antihydrogen.

Our simulations do not include radiative formation since at positron temperatures around 15 K, and at relevant densities for ATHENA, the rate of this process is negligible compared to that of the three-body recombination [17]. Also, we only calculate trajectories of single antiprotons, thus neglecting any effects of antiproton–antiproton or antiproton–antihydrogen interactions. This is justified since in the experiment the number of antiprotons injected in each bunch was small ($\leqslant 10^4$). As a rough estimate for the rate of collisions between an antihydrogen atom and other antiprotons, we assume a cross section $\sigma = \pi r_T^2$, a relative velocity $v \simeq 1000$ ms^{-1} and $N_{\bar{p}} \simeq 4000$ antiprotons distributed over a trap volume

Table 1. Radii and lengths of positron plasmas for different N_e and two different n_e. In all cases $T_e = 15$ K.

n_e (m^{-3})	N_e	Radius (mm)	Length (mm)
5×10^{13}	7.0×10^6	2.27	13.13
5×10^{13}	1.4×10^7	2.87	16.52
5×10^{13}	2.8×10^7	3.64	20.70
1×10^{15}	6.0×10^7	0.87	38.34
1×10^{15}	1.2×10^8	1.11	51.75

$V \simeq 10^{-6}$ m^3. This gives a collision rate $\sigma v N_{\bar{p}}/V \simeq 4$ s^{-1} per antihydrogen atom. The maximum life time of an antihydrogen atom is given by the time it needs to travel from the centre of the trap to the detector, which is of the order 10^{-5} s. Thus only about one antihydrogen atom in 10 000 would collide with an antiproton. This is clearly an unimportant effect. As for antiproton–antiproton collisions, we expect a similar rate since the Coulomb cross section is reduced by plasma screening.

To achieve good statistical accuracy, a large number (up to 50 000) of trajectories have been calculated for each parameter setting. Of these, only a fraction, typically 20–40%, result in a detected antihydrogen atom. This gives between 10 000 and 20 000 'events', which when grouped, for example, in 100 time bins gives an average of 100–200 events per bin. Assuming Poisson statistics, this gives a typical statistical uncertainty around 5–10%, but obviously this may be much larger when the number of events is lower, or approaches zero. The remaining trajectories end with the antiproton trapped outside the positron plasma.

3. Results and discussion

3.1. Varying the total number of positrons

In order to fully explore the density regions of interest to the experimental programmes, it was necessary to perform simulations at fixed n_e and T_e, but with varying total numbers of positrons, N_e. This would have the effect of changing the radius and length of the simulated plasma, and hence the electric field in the plasma (3), such that any quantity which is influenced by the field at the edge of the plasma will be sensitive to N_e. Table 1 shows representative values of N_e (with the consequent plasma radii and lengths) for the extreme densities simulated of 5×10^{13} m^{-3} and 1×10^{15} m^{-3}, both for $T_e = 15$ K.

Figures 3 and 4 show outputs of the simulations, namely the time dependence of the antihydrogen formation, the distribution of binding energies and the axial and transverse antihydrogen speeds, v_z and v_{tr}, for the two densities. Whilst there are clear and important differences in these parameters for the two densities (discussed below), what is relevant here is the consistency of the output at each n_e for the different values of N_e. For $n_e = 5 \times 10^{13}$ m^{-3}, there are no apparent differences in any of the parameters for the different values of N_e. Hence, there is no sensitivity at this density to the radial field at the edge of the plasma. This implies that, for v_z and v_{tr}, thermal effects dominate in this example.
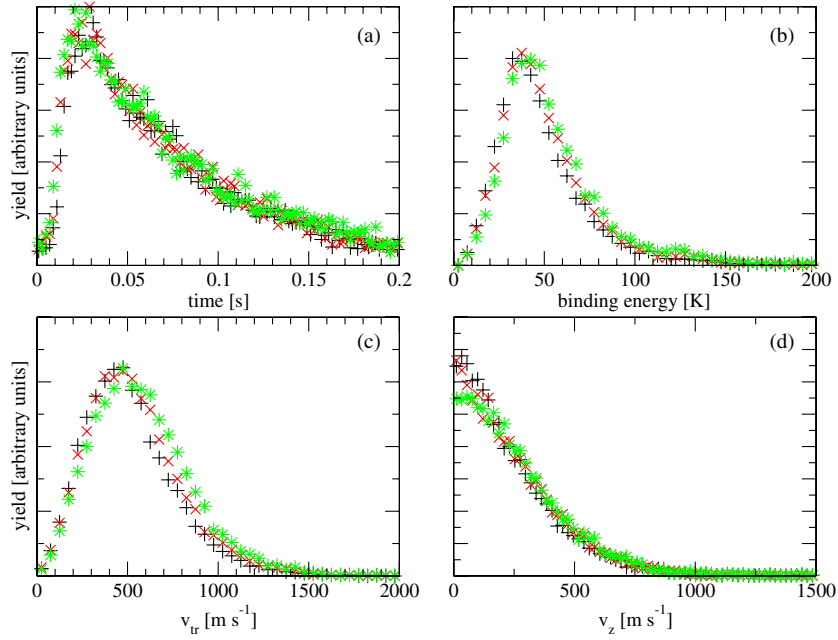
Figure 3. Simulation parameters for $n_e = 5 \times 10^{13}$ m^{-3} and $T_e = 15$ K for values of N_e of (+) 7×10^6, (×)1.4×10^7 and (∗) 2.8×10^7. (a) The time dependence of antihydrogen detection; (b) the binding energy distributions of the detected antihydrogen; (c) the antihydrogen speed distributions in the transverse plane and (d) their axial counterparts.
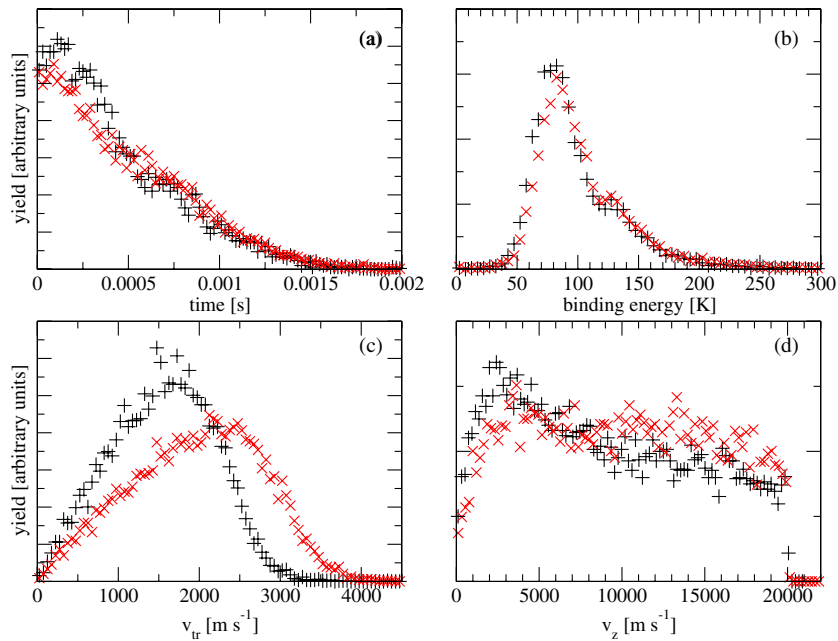

Figure 4. Simulation parameters for $n_e = 1 \times 10^{15}$ m^{-3} and $T_e = 15$ K for values of N_e of (+) 6×10^7 and (×)1.2×10^8. (a) The time dependence of antihydrogen detection; (b) the binding energy distributions of the detected antihydrogen; (c) the antihydrogen speed distributions in the transverse plane and (d) their axial counterparts.

However, at 10^{15} m^{-3} there is an effect, most notably in v_{tr}, which shifts to a higher mean value for the plasma with the largest radius. This effect is due to the fact that v_{tr} is dominated by the $\mathbf{E} \times \mathbf{B}$ drift speed (see section 3.2) of the antiproton at the radius where the anti-atom was formed, which, at the higher density, results in a noticeable effect above thermal. This must be borne in mind in the discussions below.

3.2. Time dependence of the formation of detected and ionized antihydrogen and equilibrium rates

Antiprotons can be lost through two mechanisms, both involving formation of antihydrogen. Either an antihydrogen atom is detected at the electrodes surrounding the nested Penning trap or it is field ionized before it reaches the detector.
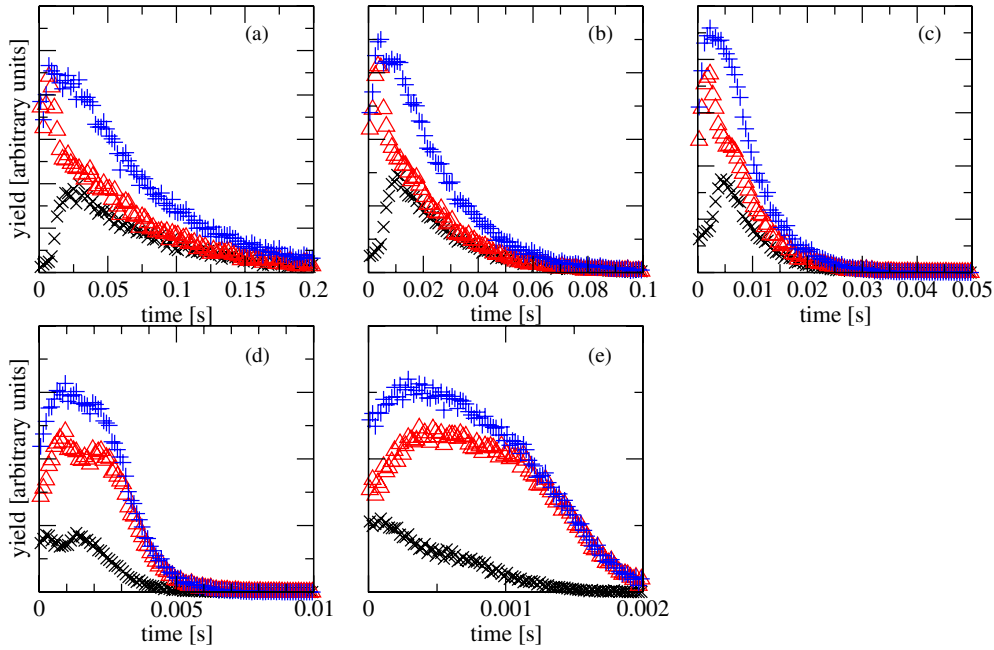
Figure 5. Simulated time dependences of the ($\times$) detected and ($\triangle$) ionized antihydrogen together with the sum of the two (+). The data are for positron densities, n_e, of (a) 5×10^{13} m^{-3}, (b) 10^{14} m^{-3}, (c) 2×10^{14} m^{-3}, (d) 5×10^{14} m^{-3} and (e) 10^{15} m^{-3}.

In this case the antiproton is likely to get trapped in the potential wells surrounding the positron plasma. We therefore define two (in general time-dependent) rates: one for detected antihydrogen λ_d and one for antiproton loss through field ionization, λ_l. These are the ratios of the number of events per unit time to the number of antiprotons in the trap, i.e.

$$\frac{dN_d(t)}{dt} = \lambda_d N(t), \tag{5}$$

$$\frac{dN(t)}{dt} = -(\lambda_d + \lambda_l)N(t), \tag{6}$$

where $N_d(t)$ is the number of antihydrogen atoms detected up to the time t, while $N(t)$ is the number of antiprotons still in the trap at time t. At long times (longer than the time for thermalization of antiprotons with the positron plasma), λ_d and λ_l approach constant values, which can be extracted from the distributions in figure 5 using equations (5) and (6).

Simulations were performed at five values of n_e in the range 5×10^{13}–10^{15} m^{-3} at $T_e = 15$ K. The variations of the antiproton loss to antihydrogen for both the detected and ionized anti-atoms, together with the sum of the two, are shown in each case in figures 5(a)–(e). Note that the timescales for each plot are different, with fully two orders of magnitude change between 5×10^{13} m^{-3} and 10^{15} m^{-3}. In all cases, the fraction of antiprotons lost due to ionized antihydrogen is larger than the fraction which escapes the plasma to be detected via annihilation. The difference increases with increasing density, as might be expected due to the increased plasma fields which field ionize a larger fraction of the nascent antihydrogen.

At densities up to and including 2×10^{14} m^{-3} there is a definite onset, presumably due to the effect of antiproton slowing in the plasma. The onset is sharper for the antihydrogen which is field ionized, probably because these very weakly bound states exit the plasma first, and extra

time is needed to achieve binding energies sufficient to survive the plasma and trap fields. In these three cases a definite equilibrium is reached, with the ionized and detected antihydrogen displaying a similar (density-dependent) decay with time which can be characterized (see below) by a single exponential curve.

At $n_e = 5 \times 10^{14}$ m^{-3} the onset is less evident and is not really visible for the detected species. Instead a large shoulder-type feature is apparent, which totally dominates the distribution at 10^{15} m^{-3}. The beginnings of this feature can also be seen in the distribution for $n_e = 2 \times 10^{14}$ m^{-3}. It is clear that as the density increases epithermal effects dominate and equilibrium may not be reached. However, it is noticeable that the detected antihydrogen rate seems to approach an equilibrium before the ionized signal.

At the higher densities and longer times, the distributions are dominated by ionized antihydrogen events. This is consistent with the observations in section 3.5 that the antiprotons quickly migrate to the plasma edge, where they are most likely to form weakly bound anti-atoms which are susceptible to ionization.

The timescales for the simulations of antihydrogen can be compared with those from the ATHENA experiment, which typically operated at positron densities just above 10^{14} m^{-3}. ATHENA found that the antihydrogen detection rate rose to a maximum after about 40 ms of mixing, and persisted for many seconds thereafter [35]. Using more dense plasmas [36], ATHENA were able to shorten the effective time over which the bulk of their antihydrogen signal was produced to a fraction of a second. However, we find that the simulated timescales are an order of magnitude, or more, shorter. Although we can offer no definitive explanation for this difference, it is likely that the discrepancy, at least in part, is due to the effects of the separation of antiprotons from the positrons due to drift-field
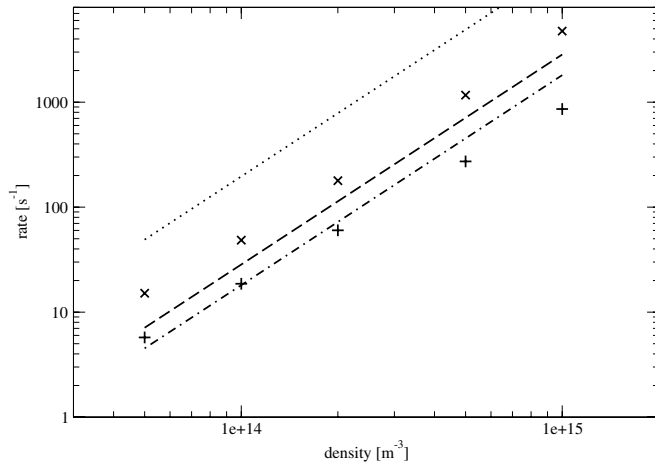
Figure 6. Equilibrium rates for the antihydrogen atoms at $T_e =$ 15 K versus positron density for detected antihydrogen λ_d (+) together with the total rate of antiproton loss λ_{tot} (×). The lines show theoretical predictions for the steady-state formation rate for $B = 0$ (dotted) [10], $B = 3$ T (dashed) [20] and $B \to \infty$ (dash-dotted) [19].

ionization of weakly bound anti-atoms, as reported here, and as observed by ATHENA [35]. The positron plasma in ATHENA was slowly (on a timescale of many seconds [15]) expanding with time during mixing, such that those antiprotons on the periphery of the cloud would eventually come into overlap with the positrons again. The effects of this were evident in a study employing a dense positron plasma [36], with a diameter smaller than that of its accompanying antiprotons.

The equilibrium rates, calculated according to equations (5) and (6), are plotted versus n_e in figure 6 and exhibit power law behaviour, $\lambda_d \propto n_e^n$, with n a constant. Fits yield $n = 1.67 \pm 0.01$. For the data displayed in figure 6, the antiprotons were launched into the positron plasma with a speed of 2×10^4 ms^{-1}, equivalent to a kinetic energy of 2 eV. Comparisons were also made with runs starting with an assumed thermal distribution, for which the fitted value of n was 1.61 ± 0.04. Thus the simulations predict that the antihydrogen detection rate should scale roughly as $n_e^{5/3}$, rather than the value of n_e^2 as expected from the basic three-body process.

We also include the total loss rate $\lambda_{tot} = \lambda_d + \lambda_l$ in figure 6. As discussed above, this rate comprises antihydrogen formation leading either to a detected anti-atom or to antiproton loss due to field ionization. Its density dependence is fitted by the power law $n_e^{1.93 \pm 0.05}$, although the fit is slightly worse than that for the detection rate. Thus, it is close to the n_e^2 scaling expected for three-body recombination in steady state. The reduced power of the detection rate must therefore mainly be due to a density-dependent selection of the antihydrogen atoms which survive to the detector.

Although the magnitude of λ_{tot} we obtain agrees better with the steady-state prediction at $B = 3$ T [20] than the predictions at $B = 0$ [10] or $B = \infty$ [19], our result is still significantly larger. This can be understood since in [20] a recombined anti-atom was defined as an anti-atom with binding energy larger than $8k_B T_e$ (the calculations at $B = 0$

[10] and $B = \infty$ [19] used similar definitions). The rate λ_{tot} on the other hand represents the rate of anti-atoms leaving the plasma, irrespective of their binding energy. Since almost all anti-atoms have a binding energy less than $8k_B T_e$ when they leave the plasma, this rate has to be larger. The rate λ_d for detected antihydrogen, i.e. with the field-ionized anti-atoms removed, is on the other hand smaller than the result in [20] at all plasma densities.

3.3. Field ionization through azimuthal drift

The difference in density scaling between the total formation rate and the detection rate shows that some density-dependent mechanism for ionization of weakly bound antihydrogen must be operating. The radial electric field equation (3) inside the plasma is indeed proportional to the plasma density and reaches its maximum at the surface of the plasma. This field can, however, not directly cause field ionization. This is because this field is radial and, according to the simulations, and intuitively, this cannot lead to break-up of the pair due to the presence of the strong axial magnetic field. On the other hand, it is also unlikely that the density-dependent selection of detected antihydrogen is due to field ionization by the axial electric field since its strength only has a weak density dependence, giving for higher densities smaller fields close to the plasma (see the axial potential in figure 1).

The simulations have revealed that ionization at the edge of the plasma proceeds via an azimuthal separation of the pair due to a small difference between the drift velocities of the positron and antiproton. The drift velocity, $\mathbf{v}_d$, of charged particles in crossed electric and magnetic fields (which is the situation here with the plasma electric field $\mathbf{E} = E_r\hat{\rho}$ and the solenoidal magnetic field $\mathbf{B} = B_z\hat{\mathbf{z}}$) can be shown to be (see e.g. [37])

$$\mathbf{v}_d = \left(-\frac{E_r}{B_z} + \frac{mE_r^2}{eB_z^3 r} \right)\hat{\phi} = (v_{d0} + \Delta v_d)\hat{\phi}, \tag{7}$$

with m the mass of the particle and $\{\hat{\rho}, \hat{\phi}, \hat{\mathbf{z}}\}$ the standard cylindrical coordinate system of the particle in the trap. The first term in (7) is the 'normal' drift of the pair, but a mass-dependent term, Δv_d, is introduced at the second order, and it is this that eventually results in the separation of the pair.

In order to get a clearer picture of field ionization, we have studied it isolated from the effect of collisional ionization. Therefore we make a simulation solely for propagation in the fields, i.e. no collisions are included. In the full simulations both ionization mechanisms of course operate simultaneously. Figure 7 shows plots of the time variation of various properties of an antihydrogen atom moving in a radial field, $E_r\hat{\rho}$ (corresponding to that of a plasma of density 10^{15} m^{-3}) and with $B_z = 3$ T. In all panels there is an abrupt change in the behaviour at the time marked by the green line, which seems to indicate the break-up of the pair. Panels (a) and (b) in figure 7 show the relative positron–antiproton coordinate **r** separated into its components along the azimuthal (i.e. the $\hat{\phi}$-component) and the radial ($\hat{\rho}$) directions of the trap. (The $\hat{\mathbf{z}}$ component is not displayed. For the two-particle system, the cylindrical coordinate system is defined relative to their centre
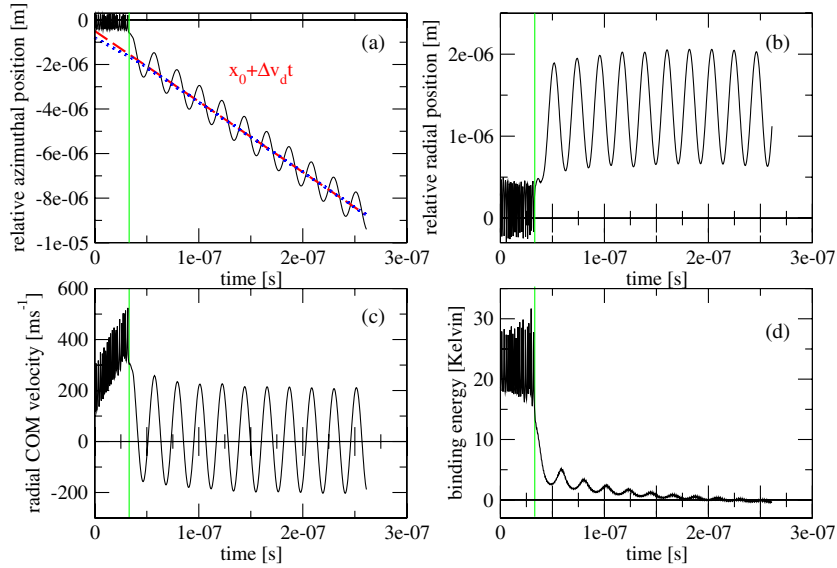
Figure 7. (a) Simulation of the time dependence of the $\hat{\phi}$-component (the component along the azimuthal coordinate of the trap) of the position of the positron relative to the antiproton. The positron is undergoing azimuthal drift in the crossed electric and magnetic fields. The dashed line is a fit based upon (7) and the dotted line is the location of the minimum of the outer potential well, $y_0 = -K_r/(eB)$; see the text. (b) The corresponding relative position along the radial coordinate of the trap ($\hat{\rho}$ component). (c) The simulated time dependence of the centre-of-mass velocity along $\hat{\rho}$. (d) The binding energy of the pair. The significance of the vertical lines is discussed in the text.

of mass.) Figure 7(a) clearly illustrates how the anti-atom is torn apart in the azimuthal direction of the trap. The dashed line is the separation given by Δv_d from (7), plus some initial separation, denoted here as x_0. Figure 7(b) shows that the radial electric field of the trap can induce an electric dipole moment (which after the break-up time becomes large since the Coulomb attraction between the particles is small) but because of the magnetic field the anti-atom cannot be ionized in this direction. The oscillations in both panels are due to the cyclotron motion of the antiproton.

Figure 7(c) shows the centre-of-mass velocity in the radial direction of the trap. While the anti-atom is tightly bound it accelerates away from the trap centre due to the centrifugal force. Once the pair separates, the radial centre-of-mass speed abruptly starts to oscillate around zero. This behaviour is characteristic of two separated charged particles, undergoing cyclotron oscillations around a constant trap radius. Figure 7(d) shows the binding energy of the atom. It should be remembered that in the presence of external fields the binding energy is not a conserved quantity. Here we chose to define it without including any contributions from the external fields, i.e. as the sum of the attractive Coulomb potential between the particles and the kinetic energy associated with the positron motion relative to the antiproton. Before the break-up, the binding energy oscillates around ∼23 K showing that the system is indeed a loosely bound anti-atom. After the break-up, the binding energy gradually drops to zero.

Our interpretation of this is as follows. The internal dynamics, given by the positron–antiproton relative coordinate, **r**, of an antihydrogen atom in static electric and magnetic fields can be described by the effective potential [30, 38]

$$V(\mathbf{r}) = \frac{1}{2M}(\mathbf{K} - e\mathbf{B} \times \mathbf{r})^2 - \frac{e^2}{4\pi\epsilon_0 r} - e\mathbf{E} \cdot \mathbf{r}, \qquad (8)$$

where M is the mass of the anti-atom. The pseudo-momentum $\mathbf{K} = M\dot{\mathbf{R}} + e\mathbf{B} \times \mathbf{r}$ gives a coupling to the centre-of-mass coordinate **R**. For static fields, **K** is a conserved quantity, facilitating a 'pseudo-separation' between centre-of-mass and internal motion. The first term in $V(\mathbf{r})$ will thus create a shallow outer potential well, located at $\mathbf{r} = -\mathbf{B} \times \mathbf{K}/(eB^2)$. Atoms bound in this outer well are called *giant dipole states*.

Inside the positron plasma the magnetic field is static, but the electric field grows radially according to (3). The pseudo-momentum is therefore *not* a conserved quantity. As described above, this combination of electric and magnetic fields makes charged particles rotate around the axis of the trap with a speed given by (7). The pseudo-momentum is separated into its radial and azimuthal components, $\mathbf{K} = K_r\hat{\rho} + K_\phi\hat{\phi}$ in a coordinate system rotating with the centre of mass. One finds

$$\dot{K}_r = MR\dot{\phi}^2 + (eB_z\dot{\phi} + eE_r/R)x, \qquad (9)$$

where $\dot{\phi}$ is the angular speed of the centre of mass, E_r is evaluated at the radius R and $\mathbf{r} = x\hat{\rho} + y\hat{\phi}$. When the Coulomb potential is negligible compared to interaction with the external fields, as when the anti-atom is bound in a giant dipole state, both particles will drift as free charged particles, giving $\dot{\phi} \simeq -E_r/(B_z R)$. Hence, to first order $\dot{K}_r = ME_r^2/(RB_z^2)$, that is, the radial component of the pseudo-momentum grows due to the centrifugal force. Thus the minimum of the outer potential well will drift away with a speed $\sim \dot{K}_r/(eB_z) = ME_r^2/(eB_z^3 R)$. Neglecting terms of order electron mass divided by proton mass, this is the same as the difference Δv_d in the drift speed between the antiproton and the positron in (7). Hence, the slight difference in drift speed will cause any antihydrogen atoms bound in a giant dipole state to grow in the azimuthal direction.

At the time corresponding to the vertical line shown in all panels of figure 7, around 350 ns, the atom goes from a
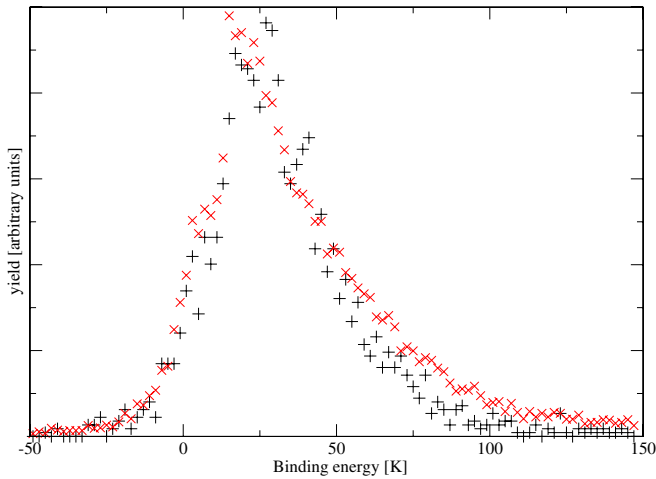
Figure 8. The binding energy distributions at positron densities of (×) 10^{15} m^{-3} and (+) 5×10^{13} m^{-3} as extracted from the simulations at the point at which the antihydrogen atoms leave the plasma. These results were obtained using antiprotons initialized in thermal equilibrium with the 15 K plasma.
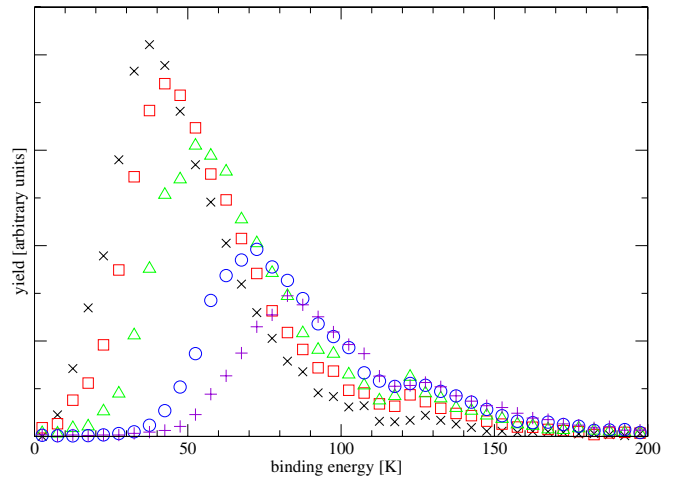

Figure 9. The binding energy distribution of the antihydrogen on detection at positron densities of (×) 5×10^{13} m^{-3}, (□) 10^{14} m^{-3}, (△) 2×10^{14} m^{-3}, (○) 5×10^{14} m^{-3} and (+) 10^{15} m^{-3}. T_e was 15 K in each case.

'normal' state to a giant dipole state. Panel (a) of figure 7 includes a fit of the azimuthal separation after the transition to the speed Δv_d, along with the location $y_0 = -K_r/(eB_z)$ of the minimum of the outer potential well. This dipole continues to grow because of the difference in the drift speed. The simulation ends when the positron leaves a pre-defined box with the side of length 10 μm around the antiproton. In the simulation, this marks the anti-atom as ionized. However, the anti-atom is certain to be ionized already at the time of the start of the breakup marked by the green line in figure 7.

3.4. Antihydrogen-binding energies

The binding energy, E_b, of the antihydrogen, defined as in section 3.3, is also an output of the program. Figure 8 shows the simulated binding energy distributions just outside the positron plasma at the highest and lowest densities investigated, namely 5×10^{13} m^{-3} and 10^{15} m^{-3}. Interestingly, there is very little difference between the two, with perhaps a slight preponderance of more tightly bound states at the higher n_e. The distributions peak around 25 K and very few antihydrogen atoms seem to be bound by more than 100 K. As described above in section 2, the initial condition for the anti-atoms requires a binding energy of at least $k_B T_e$, which explains the reduced yield above this binding energy. The distributions each have a small tail of states extending to binding energies below zero, i.e. states which in the absence of external fields are unbound. (Such states have been discussed previously in [25].) The binding energy of these atoms have been reduced due to collisions with positrons. They can briefly be held together by the external fields, but will eventually dissociate, usually through the mechanism involving transition to a giant dipole state described in section 3.2. As shown below, none of these very loosely bound anti-atoms survive to the detector. The details of their distribution is therefore of limited interest to us.

The situation shown in figure 8 should be contrasted with the distribution of binding energies of the antihydrogen when detected, shown in figure 9 for all five values of n_e investigated here. There is a clear shift to deeper E_b with increasing density. This is qualitatively in accord with expectations since the electric field (and induced separation as described above) will increase with n_e, causing the more weakly bound states to be field ionized. An estimate of the onset of the binding energy distribution can be obtained by assigning this energy to one half of the value at the peak for each n_e. This reveals that the onset is well described by a power law, scaling as $n_e^{0.35}$.

3.5. Evolution of antihydrogen formation positions in the plasma

The fraction of time that an antiproton spends bound to a positron as an antihydrogen atom is usually small; even at $n_e = 10^{15}$ m^{-3} this is less than 1% of the total time. Thus the frequency of destruction is much faster than that for formation, which might be expected given that collisions between the nascent antihydrogen atoms and the positrons in the plasma are likely to proceed with very large cross sections. The same physics underlying the trends of collisions of Rydberg species with charged projectiles, which results in the cross sections scaling with the geometric area of the atoms [39], can be applied here. For instance if the destruction cross section is $\sim 10^{-14}$ m^2 [39] with $n_e = 10^{15}$ m^{-3} and antihydrogen speeds $> 10^3$ ms^{-1} (see figures 12 and 13) then the destruction rate will be greater than 10^4 s^{-1} per anti-atom. The fraction of time a typical antiproton spends as antihydrogen seems to increase roughly as n_e. This is to be expected if the destruction rate is much larger than the formation rate. In this case, the equilibrium number of antihydrogens is proportional to the ratio of the three-body formation rate, proportional to n_e^2, and to the destruction rate, proportional to n_e, which gives an overall proportionality to n_e.

However, the formation and destruction of antihydrogen does have a profound influence upon the time dependence of
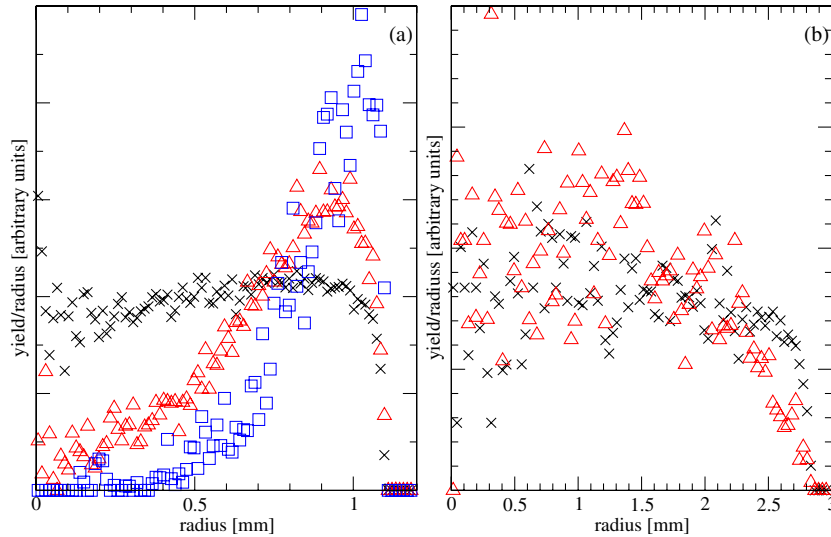
Figure 10. The radial dependence of the distribution of antihydrogen formation positions (including both detected and ionized antihydrogen): (a) $n_e = 10^{15}$ m^{-3} integrated over time intervals ($\times$) < 0.1 ms; ($\triangle$) 0.4–0.5 ms and ($\square$) > 1.0 ms. (b) $n_e = 5 \times 10^{13}$ m^{-3} for the two time intervals, ($\times$) < 25 ms and ($\triangle$) > 100 ms. These results were obtained using antiprotons initialized in thermal equilibrium with the 15 K plasma.

the radial distribution of the antiprotons. If an antiproton does not form antihydrogen, it stays at a fixed radial position as the simulation proceeds, due to the presence of the 3 T magnetic field. However, when it neutralizes it may drift across the field to a larger radius, where it can be field ionized. The nett effect of this is most obvious at the higher positron densities. Figure 10(a) shows the radial distribution $(1/r)\,dN_p/dr$ of antiprotons versus radial position in the plasma in three different time intervals for the positron density of 10^{15} m^{-3}. It is clear that as time proceeds, the antiprotons move to the outer edge of the plasma, and more-or-less none remain in the central region. At the lower density of 5×10^{13} m^{-3}, shown in figure 10(b), this effect is not present due to the much lower frequency with which the antihydrogen is destroyed.

This effect is important for efforts to trap antihydrogen since the overall kinetic energy of the antihydrogen will unavoidably contain a component from the $\mathbf{E} \times \mathbf{B}$ drift of the antiproton prior to formation. From (3), this is proportional to the radial position of formation. If the antiprotons reside close to the outskirts of the positron plasma, as suggested by our data, the kinetic energy of the antihydrogen is likely to be in excess of the realizable magnetic trap depths. The latter are about 1 K for ground-state antihydrogen [4, 5], but scale with the orbital angular momentum if excited states are involved.

3.6. Radii of antihydrogen formation and transverse speeds

At high densities, the ionizations just outside the plasma seem to be delayed events resulting from the collisional creation of unstable states inside the plasma, but with the positron and the antiproton separating on the outskirts of the plasma. Once this occurs, the antiproton may become trapped in a side well of the nested trap, or may be returned to the plasma. The antiprotons which become field ionized and trapped result from antihydrogen atoms which formed very close to the edge of

the plasma. The difference in radius, Δr, between the point of antihydrogen formation and where it left the plasma is shown in figure 11. Figure 11(a) shows the case for $n_e = 10^{15}$ m^{-3}, whilst figure 11(b) is for 5×10^{13} m^{-3}. Whilst both graphs are of similar form, showing that the antihydrogen atoms which end up being ionized have usually travelled a very short distance inside the plasma, the effect is much more pronounced at the higher density. By contrast, the antihydrogen atoms which escape the plasma and are detected are formed much more uniformly throughout the plasma.

These observations are understandable since the antihydrogen atoms which are field ionized are the more weakly bound cohort, which we see are formed preferentially towards the edge of the plasma. Less time is spent in the plasma for those anti-atoms formed nearer the edge, and hence they will undergo fewer collisions (which can either ionize the anti-atom, or drive it to a more deeply bound state). Thus, these atoms are more likely to be field ionized as they exit the plasma. The antihydrogen which typically survives the plasma field is formed over a broad range of positions within the plasma and is already deeply enough bound on formation to survive. This could explain the fact that there is no peak in these distributions at larger Δr.

A related observation is as follows. The transverse speed, v_{tr}, distributions for the antihydrogen atoms which are detected and for those which are eventually field ionized are shown in figures 12(a) and (b) (for $n_e = 10^{15}$ m^{-3} and 5×10^{13} m^{-3}, respectively). In this plane the speed of the antiprotons will be thermal, plus that due to the $\mathbf{E} \times \mathbf{B}$ drift. Since, from (3) and (7), the latter depends upon the radius, the transverse speed of the antihydrogen leaving the plasma may, depending upon the relative size of the drift and thermal speeds, be characteristic of the radius at which it was formed. Figure 12(a) shows, that at the highest n_e, the antihydrogen atoms which field ionize have a larger v_{tr} than those which survive. This is because the former are predominantly formed at larger radii,
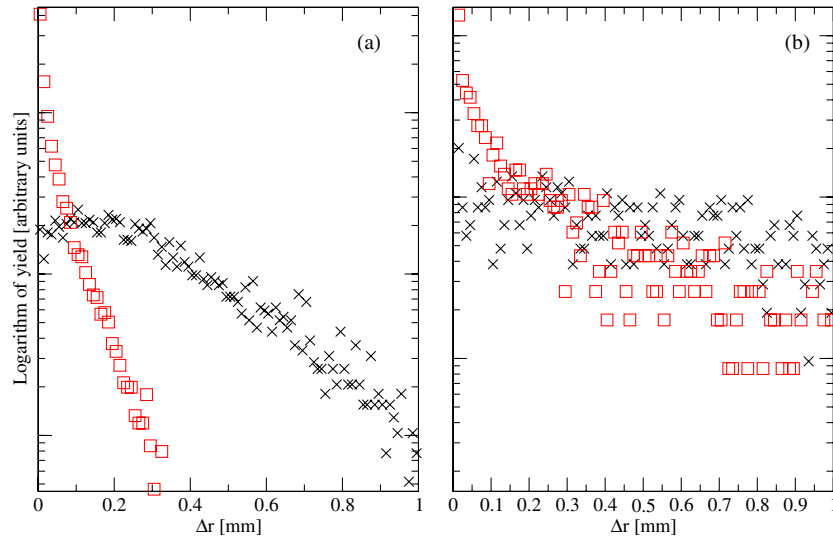
Figure 11. The distribution of the difference in radius between the point of formation of antihydrogen atoms and the point at which they left the positron plasma, for ($\times$) detected and ($\square$) ionized antihydrogen, (a) $n_e = 10^{15}$ m^{-3}, (b) $n_e = 5 \times 10^{13}$ m^{-3}. These results were obtained using antiprotons initialized in thermal equilibrium with the 15 K plasma.
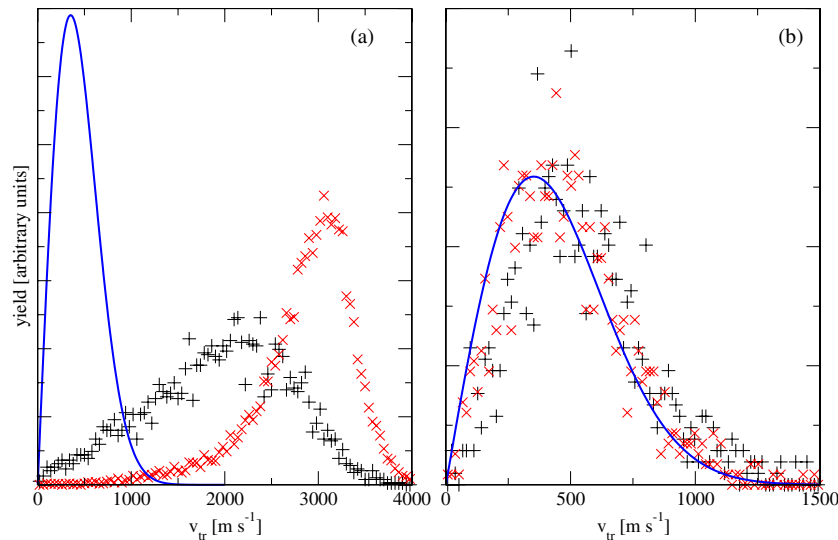

Figure 12. Simulated distribution of transverse speeds of the detected (+) and field ionized ($\times$) antihydrogen atoms. The solid lines are Maxwell–Boltzmann speed distributions corresponding to a temperature of 15 K. (a) $n_e = 10^{15}$ m^{-3}, (b) $n_e = 5 \times 10^{13}$ m^{-3}. These results were obtained using antiprotons initialized in thermal equilibrium with the 15 K plasma.

and therefore have a higher drift speed. At $n_e = 5 \times 10^{13}$ m^{-3}, however, there is no noticeable difference between the two v_{tr} distributions, which are dominated by thermal effects. A 15 K Maxwell–Boltzmann distribution is shown in figure 12 for comparison and is nearly coincident with the simulated distribution at $n_e = 5 \times 10^{13}$ m^{-3}.

3.7. Kinetic energies

We have computed the axial speeds, v_z, and the overall kinetic energies for the antihydrogen atoms which survive the plasma and are detected at each density and are shown in figure 13 (see also figures 3 and 4). Recall that in the simulation the antiprotons are injected into the positron plasma with an axial speed of 2×10^4 ms^{-1}. There are marked changes in

v_z with density. The more rapid formation of antihydrogen by epithermal antiprotons at the higher densities results in a wide spread of axial speeds, extending right up to that of the antiproton on injection. At 5×10^{13} m^{-3}, the kinetic energy distribution peaks just above 15 K and is very close to the thermal distribution. At the higher densities, the kinetic energy peaks at progressively higher energies with, at $n_e = 10^{15}$ m^{-3}, the distribution extending up to the injection energy.

3.8. Axial distribution of antihydrogen annihilations

The z-distribution (i.e. the distribution along the axis) of the antihydrogen annihilations is shown in figure 14 at each n_e. The data have been convoluted with a Gaussian with 4 mm width to allow for the finite resolution of the detectors in
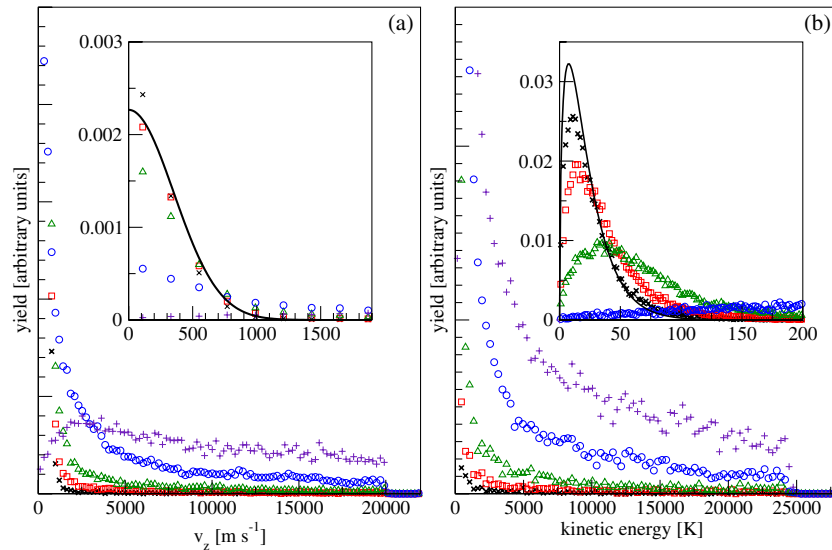
Figure 13. (a) Simulated antihydrogen axial speeds at (×) $n_e = 5 \times 10^{13}$ m^{-3}, ($\square$) $n_e = 10^{14}$ m^{-3}, ($\triangle$) $n_e = 2 \times 10^{14}$ m^{-3}, ($\circ$) $n_e = 5 \times 10^{14}$ m^{-3} and (+) $n_e = 10^{15}$ m^{-3}. The inset details the behaviour at low speeds. (b) Antihydrogen kinetic energies, expressed in units of kelvin. Here the inset shows the behaviour at low energies, which is mainly of relevance for the three lower densities. In both insets, a 15 K distribution is included for comparison.
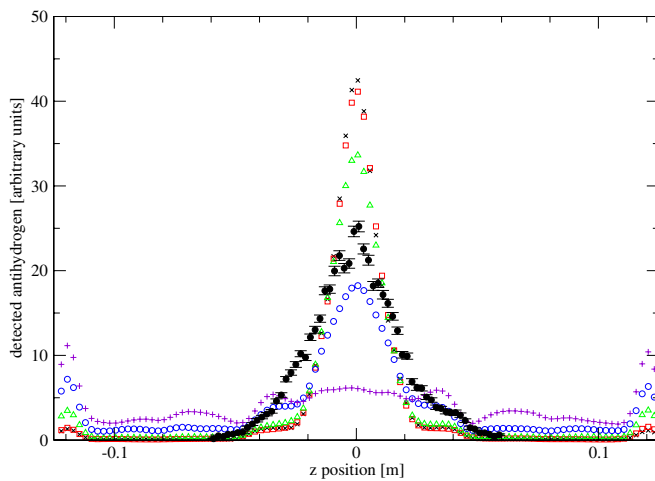

Figure 14. The axial distribution of antihydrogen annihilation at each density: (×) $n_e = 5 \times 10^{13}$ m^{-3}, ($\square$) $n_e = 10^{14}$ m^{-3}, ($\triangle$) $n_e = 2 \times 10^{14}$ m^{-3}, ($\circ$) $n_e = 5 \times 10^{14}$ m^{-3} (+) $n_e = 10^{15}$ m^{-3} and (●) experimental data at $n_e = 1.7 \times 10^{14}$ m^{-3} [22].

the experiment. These plots are striking in their density dependence, as is the notable difference between them and the distribution extracted by the ATHENA collaboration [22], which is also included in figure 14. The simulated z-distribution at $n_e = 2 \times 10^{14}$ m^{-3} is narrower than the experimental result from [22], where a similar density, $n_e = 1.7 \times 10^{14}$ m^{-3}, is quoted. In [22], the broad axial distribution was attributed to the epithermal formation of antihydrogen. Our simulations indicate that at $n_e = 1.7 \times 10^{14}$ m^{-3} and $T_e = 15$ K the epithermal formation rate is not high enough to explain the axial distribution measured in [22].

At the higher densities at $T_e = 15$ K, the antihydrogen is, as discussed in section 3.7, formed promptly and mostly by epithermal antiprotons with significant axial speeds. Thus, the

distributions are very broad, with few anti-atoms annihilating near $z = 0$. The peaks present at $z = \pm 0.12$ m are an artefact in that these positions are the outer axial borders of the simulated cylindrical volume. Nevertheless, this indicates that at low positron temperatures and high densities, the antihydrogen is strongly axially peaked.

As the density is lowered and antihydrogen formation via the three-body mechanism slows preferentially with respect to antiproton slowing down in the positrons, the distribution becomes more centred around $z = 0$, as would be expected for a thermal ensemble. At $n_e = 5 \times 10^{13}$ m^{-3}, 94% of the distribution is contained in the central peak. The side wings on the central distribution, extending from $z \simeq \pm 0.02$ m, are positioned at electrodes which adjoin the central electrode of the trap. The transition between electrodes coincide with regions of high electric field. This will result in additional field ionization of antihydrogen atoms and hence a reduced number of antihydrogen atoms reaching the next electrode.

4. Conclusions

Detailed simulations of antihydrogen formation have been performed for varying n_e at $T_e = 15$ K, including the populations of antihydrogen detected after reaching the wall of the Penning trap, and those field ionized.

We find the time dependence of the rates for both detected and ionized species to be increasingly influenced by epithermal effects as n_e is increased. (The latter arises due to the manner of $\bar{p}$ injection into the positron plasma as applied in the ATHENA experiment.) Equilibrium rates could be isolated for the detected antihydrogen atoms and were found to vary as $\sim n_e^{1.7}$, compared to the underlying n_e^2 dependence of reaction (2). The difference was attributed to field ionization due to the inherent radial electric field of the plasma. The field ionization of weakly bound antihydrogen which occurs in the Penning traps

used (which typically have magnetic fields in the tesla region) was found to be due to a second-order effect which induces a mass-dependent azimuthal drift which separates the pair. The distribution of the binding energy of the detected antihydrogen atoms was investigated at various n_e, revealing a shift towards deeper levels as the density is increased. This is caused by the removal of weakly bound states due to the increase of the radial plasma electric field with n_e. The role of the field ionization of nascent antihydrogen atoms in causing cross-plasma drift was highlighted. At the higher n_e, this resulted in preferential formation of very weakly bound antihydrogen near the plasma edge, which is subsequently broken up as it leaves the plasma.

The influence of the positron density on the transverse (to the magnetic field) and axial speeds and kinetic energies was deduced. As n_e is increased epithermal effects, due to the residual kinetic energy of the $\bar{p}$, dominate the axial speeds, whilst the effect of the $\mathbf{E} \times \mathbf{B}$ rotation of the positron plasma has an increasing effect on the transverse speeds. Only at the lowest density simulated (at $T_e = 15$ K) does the kinetic energy distribution of the antihydrogen approach thermal. Similarly, the axial distribution of antihydrogen annihilation is dramatically dependent upon n_e, with the axial speed dominant at high n_e. The simulated rates of antihydrogen formation and detection are far higher than those found in the ATHENA experiment. At the moment we have no explanation for the discrepancy though we note that the three-body reaction is strongly dependent upon T_e, and that ATHENA could not directly measure the base temperature of the positron plasmas used in their experiment.

Acknowledgments

References

[1] Amoretti M *et al* 2002 *Nature* **419** 456
[2] Gabrielse G *et al* 2002 *Phys. Rev. Lett.* **89** 213401
[3] Robicheaux F 2008 *J. Phys. B: At. Mol. Opt. Phys.* **41** 192001
[4] Andresen G *et al* 2007 *Phys. Rev. Lett.* **98** 023402
[5] Gabrielse G *et al* 2007 *Phys. Rev. Lett.* **98** 113002
[6] Pritchard D E 1983 *Phys. Rev. Lett.* **51** 1336
[7] Saitoh H, Mohri A, Enomoto Y, Kanai Y and Yamazaki Y 2008 *Phys. Rev.* A **77** 051403
[8] Kellerbauer A *et al* 2008 *Nucl. Instrum. Methods Phys. Res.* B **266** 351
[9] Holzscheiter M H, Charlton M and Nieto M M 2004 *Phys. Rep.* **402** 1
[10] Mansbach P and Keck J 1969 *Phys. Rev.* **181** 275
[11] Müller A and Wolf A 1997 *Hyperfine Interact.* **109** 233
[12] Amoretti M *et al* 2004 *Phys. Lett.* B **578** 23
[13] Gabrielse G, Rolston S, Haarsma L and Kells W 1988 *Phys. Lett.* A **129** 38
[14] Amoretti M *et al* 2003 *Phys. Rev. Lett.* **91** 055001
[15] Amoretti M *et al* 2003 *Phys. Plasma* **10** 3056
[16] Amoretti M *et al* 2004 *Phys. Lett.* B **583** 59
[17] Stevefelt J, Boulmer J and Delpech J-F 1975 *Phys. Rev.* A **12** 1246
[18] Fujiwara M C *et al* 2008 *Phys. Rev. Lett.* **101** 053401
[19] Glinsky M E and O'Neil T M 1991 *Phys. Fluids* B **3** 1279
[20] Robicheaux F and Hanson J D 2004 *Phys. Rev.* A **69** 010701
[21] Robicheaux F 2004 *Phys. Rev.* A **70** 022510
[22] Madsen N *et al* 2005 *Phys. Rev. Lett.* **94** 033403
[23] Gabrielse G *et al* 2004 *Phys. Rev. Lett.* **93** 073401
[24] Pohl T, Sadeghpour H R and Gabrielse G 2006 *Phys. Rev. Lett.* **97** 143401
[25] Correa C E, Correa J R and Ordonez C A 2005 *Phys. Rev.* E **72** 046406
[26] Hu S X, Vrinceanu D, Mazevet S and Collins L A 2005 *Phys. Rev. Lett.* **95** 163402
[27] Vrinceanu D, Hu S X, Mazevet S and Collins L A 2005 *Phys. Rev.* A **72** 042503
[28] Robicheaux F 2006 *Phys. Rev.* A **73** 033401
[29] Topçu T and Robicheaux F 2006 *Phys. Rev.* A **73** 043405
[30] Vrinceanu D, Granger B E, Parrott R, Sadeghpour H R, Cederbaum L, Mody A, Tan J and Gabrielse G 2004 *Phys. Rev. Lett.* **92** 133402
[31] Bass E M and Dubin D H E 2009 *Phys. Plasmas* **16** 012101
[32] Dubin D H E and O'Neil T M 1999 *Rev. Mod. Phys.* **71** 87
[33] Nersisyan H B, Walter M and Zwicknagel G 2000 *Phys. Rev.* E **61** 7022
[34] Hurt J L, Carpenter P T, Taylor C L and Robicheaux F 2008 *J. Phys. B: At. Mol. Opt. Phys.* **41** 165206
[35] Amoretti M *et al* 2004 *Phys. Lett.* B **590** 133
[36] Funakoshi R *et al* 2007 *Phys. Rev.* A **76** 012713
[37] Davidson R C 1990 *An Introduction to the Physics of Nonneutral Plasmas* (Reading, MA: Addison-Wesley)
[38] Dippel O, Schmelcher P and Cederbaum L S 1994 *Phys. Rev.* A **49** 4415
[39] Gallagher T F 1994 *Rydberg Atoms* (Cambridge: Cambridge University Press)